

# Calculating the initial energy density in heavy ion collisions by including the finite nuclear thickness

Todd Mendenhall\* and Zi-Wei Lin†

*Department of Physics, East Carolina University, Greenville, NC 27858, USA*

(Dated: February 16, 2021)

The initial energy density produced in heavy ion collisions can be estimated with the Bjorken energy density formula after choosing a proper formation time  $\tau_F$ . However, the Bjorken formula breaks down at low energies because it neglects the finite nuclear thickness. Here we include both the finite time duration and finite longitudinal extension of the initial energy production. When  $\tau_F$  is not too much smaller than the crossing time of the two nuclei, our results are similar to those from a previous study that only considers the finite time duration. In particular, we find that at low energies the initial energy density has a much lower maximum value but evolves much longer than the Bjorken formula, while at large-enough  $\tau_F$  and/or high-enough energies our result approaches the Bjorken formula. We also find a qualitative difference in that our maximum energy density  $\epsilon^{\max}$  at  $\tau_F = 0$  is finite, while the Bjorken formula diverges as  $1/\tau_F$  and the previous result diverges as  $\ln(1/\tau_F)$  at low energies but as  $1/\tau_F$  at high energies. Furthermore, our solution of the energy density approximately satisfies a scaling relation. As a result, the  $\tau_F$ -dependence of  $\epsilon^{\max}$  determines the  $A$ -dependence, and the weaker  $\tau_F$ -dependence of  $\epsilon^{\max}$  in our results at low energies means a slower increase of  $\epsilon^{\max}$  with  $A$ .

## I. INTRODUCTION

The quark-gluon plasma (QGP) has been created in relativistic heavy ion collisions [1–5]. In the study of QGP properties, a key variable is the energy density produced in such collisions. The maximum value and time evolution of the produced energy density affect the trajectory of an event on the temperature-baryon chemical potential plane. For lower collision energies such as those in the Beam Energy Scan program at RHIC [6–9], the event trajectories relative to the location of the possible QCD critical point [10, 11] could significantly affect the experimental observables and their sensitivities to the critical point [10, 12]. For hydrodynamic models, the initial energy density including its spatial and temporal dependences [13–15] is an essential input for the subsequent hydrodynamical evolution of the dense matter.

The Bjorken energy density formula [16] is a convenient way to estimate the initial energy density averaged over the transverse area of a relativistic heavy ion collision:

$$\epsilon_{Bj}(t) = \frac{1}{t A_T} \frac{dE_T}{dy}. \quad (1)$$

In the above,  $A_T$  is the transverse overlap area of the two nuclei, and  $dE_T/dy$  is the transverse energy rapidity density at mid-rapidity (for estimating the initial energy density in the central region), which is often taken as the experimental  $dE_T/dy$  value in the final state. Because this formula diverges as  $t \rightarrow 0$ , one must choose a non-zero initial time, usually by assuming a finite formation time  $\tau_F$  for the produced particles. Note that the

Bjorken energy density formula assumes that all initial particles are produced at  $t = 0$  and  $z = 0$  before they start to propagate and later become on-shell. Therefore it is valid at high energies where the Lorentz-contracted nuclear thickness is negligible compared to the formation time, while it is expected to break down at low energies when the finite nuclear thickness becomes comparable to or larger than the formation time [5]. For central nucleus-nucleus collisions, it takes the following finite time in the hard sphere model of the nucleus for two identical nuclei of mass number  $A$  to completely cross each other in the center-of-mass frame:

$$d_t = \frac{2R_A}{\sinh y_{cm}}, \quad (2)$$

where  $y_{cm}$  is the rapidity of the projectile nucleus. For central Au+Au collisions at  $\sqrt{s_{NN}} = 50$  GeV, for example,  $d_t \approx 0.5$  fm/c is comparable to the usual value of the parton formation time when we take  $R_A = 1.12A^{1/3}$  fm as the nuclear radius. Therefore we may expect the Bjorken formula to break down for central Au+Au collisions at  $\sqrt{s_{NN}} \lesssim 50$  GeV [17].

A previous study by one of us [17] extended the Bjorken energy density formula by considering that the initial energy is produced over a finite duration time  $[0, d_t]$ . Its analytical result approaches the Bjorken formula at high energies. At low energies, however, it finds that the maximum energy density  $\epsilon^{\max}$  reached is much lower but the time evolution of the energy density (e.g., as measured by the time duration when the energy density stays above  $\epsilon^{\max}/2$ ) is much longer in comparison with the Bjorken formula. In addition, the maximum energy density in the low-energy limit depends on  $\ln(1/\tau_F)$ , therefore at low energies it is much less sensitive to the uncertainty of the formation time than the Bjorken formula, which energy density depends on  $1/\tau_F$ .

However, the analytical method of the previous study [17] did not take into account the finite longitudinal

\* mendenhallt16@students.ecu.edu

† linz@ecu.edu

width (in  $z$ ) of the initial energy production. In this work we include both the finite duration time and the finite  $z$ -width of the initial energy production. We then study the time evolution of the produced initial energy density in the central spacetime-rapidity region (i.e.,  $\eta_s \approx 0$ ) in the center-of-mass frame of central collisions of two identical nuclei. Note that as in the previous study we neglect subsequent interactions among the produced particles, which can be modeled by transport models [18, 19] or hydrodynamic models [13, 14]; we only study the energy produced from primary collisions between nucleons from the projectile and target nuclei.

## II. METHOD

We begin by examining in Fig. 1 the crossing of two identical relativistic nuclei traveling along the  $\pm z$  directions with speed  $\beta = \tanh y_{cm}$ . As the nuclei cross each other, the full  $z$ -width of the overlap region first increases from 0 at  $t = 0$  to  $\beta d_t$  at  $t = d_t/2$  and then decreases back to 0 at  $t = d_t$ . We refer to this rhombus (the area surrounded by the four dashed lines) as the production area because it covers the area of primary collisions in the  $z-t$  plane [20, 21]. For simplicity, in this study we neglect the transverse expansion of the overlap volume as well as the slowing down of participant nucleons during the primary collisions, as done in the Bjorken energy density formula [16] and the previous extension study [17].

We are interested in the initial energy in the narrow region  $z \in [-d, d]$  within the transverse overlap area  $A_T$  at time  $t$ . An initial parton can be produced at  $z$ -coordinate  $z_0$  and time  $x$ , i.e., at point  $(z_0, x)$ , within the production area, and it is then assumed to propagate with its velocity until it is formed after a formation time  $t_F$ . For a parton produced at time  $x$  to be within the narrow range  $z \in [-d, d]$  at time  $t$ , its rapidity  $y$  must satisfy the following condition:

$$\frac{-d - z_0}{t - x} \leq \tanh y \leq \frac{d - z_0}{t - x}. \quad (3)$$

Therefore, in the limit  $d \rightarrow 0$  the rapidity and its allowed range become

$$y \rightarrow y_0 = \tanh^{-1} \left( \frac{-z_0}{t - x} \right), \quad \Delta y = \frac{2d \cosh^2 y}{t - x}. \quad (4)$$

So the initial energy density averaged over the transverse area at time  $t$  is

$$\begin{aligned} \epsilon(t) &= \frac{1}{2dA_T} \iint_S dx dz_0 \frac{d^3 m_T}{dx dz_0 dy} \Delta y \cosh y \\ &= \frac{1}{A_T} \iint_S \frac{dx dz_0}{t - x} \frac{d^3 m_T}{dx dz_0 dy} \cosh^3 y_0. \end{aligned} \quad (5)$$

In the above,  $m_T$  is the transverse mass that is the same as the transverse energy  $E_T$  at  $y = 0$ . We use the notation  $m_T$  in this study to differentiate our  $dm_T/dy$  from

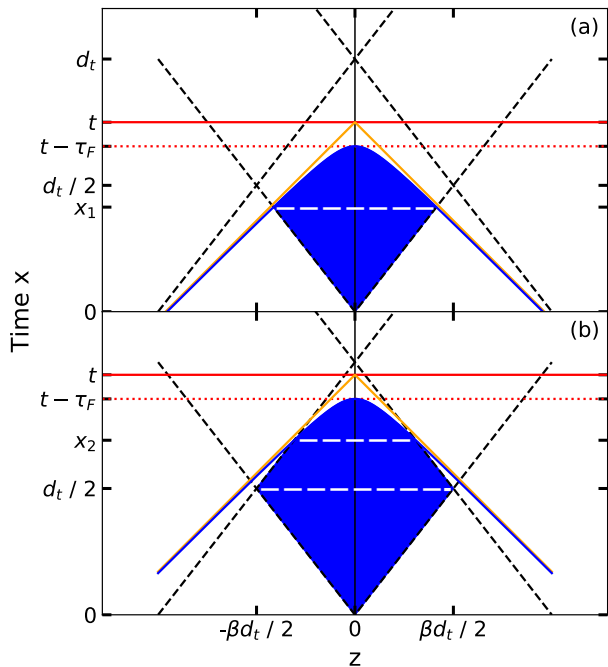


FIG. 1. Schematic diagram for the crossing of two identical nuclei, where partons can be produced anywhere inside the rhombus, for (a) the first and (b) the second piecewise solution in Table I. The solid diagonal lines represent the light cone boundaries for partons that can reach  $z \approx 0$  at time  $t$ , while the hyperbola represents the boundary of these partons after considering the formation time  $t_F = \tau_F \cosh y$ .

the experimentally measured  $dE_T/dy$  from the PHENIX Collaboration [22].

The limits of integration in Eq.(5) that determine the integration area  $S$  depend on time  $t$ . First, any  $(z_0, x)$  point needs to be within the production area, shown in Fig. 1 as the diamond-shaped area formed by the four dashed lines in each panel. Secondly, the light cone limits the production points of allowed partons below the two diagonal solid lines in each panel of Fig. 1. Finally, a parton needs to be formed by time  $t$  due to its finite formation time. Now we take the formation time of a parton in the center-of-mass frame as

$$t_F = \tau_F \cosh y, \quad (6)$$

i.e., a proper formation time  $\tau_F$  multiplied by a time-dilation factor. For a parton produced at point  $(z_0, x)$  that would reach point  $(\approx 0, t)$  and contribute to Eq.(5), its formation time is  $\tau_F \cosh y_0$ . Therefore any allowed production point needs to be below a formation time hyperbola, which is given by

$$x = t - \sqrt{z^2 + \tau_F^2}. \quad (7)$$

Note that for finite  $\tau_F$  this formation time requirement is always stricter than the light cone requirement, while for  $\tau_F = 0$  the hyperbola reduces to the light cone boundaries.

Since the integration limits of  $(z_0, x)$  in Eq.(5) depend on time, our solution of the energy density  $\epsilon(t)$  is a piecewise function in time. We now consider a more general case than Fig. 1 in that the crossing of two nuclei starts at time  $t_1$  and ends at time  $t_2$  and thus the rhombus production area is bound by the  $z = \pm\beta(x - t_1)$  and  $z = \pm\beta(x - t_2)$  lines. Then we summarize the integration limits in Table I, noting that  $\epsilon(t) = 0$  for  $t \in [0, t_1 + \tau_F]$ . In the table,  $t_a$  is the observation time when the formation time hyperbola intersects the two middle vertices of the production area at  $(z_0, x) = (\pm\beta t_{21}/2, t_{\text{mid}})$ :

$$t_a = t_{\text{mid}} + \sqrt{\tau_F^2 + \left(\frac{\beta t_{21}}{2}\right)^2}, \quad (8)$$

where we define

$$t_{21} = t_2 - t_1, \quad t_{\text{mid}} = (t_1 + t_2)/2. \quad (9)$$

The first piecewise solution is for time  $t \in [t_1 + \tau_F, t_a]$ , where the formation time hyperbola intersects the lower boundaries of the production area, i.e., the  $z = \pm\beta(x - t_1)$  lines, at time  $x_1$  that is given by

$$x_i = \frac{t - \beta^2 t_i - \sqrt{\beta^2 [(t - t_i)^2 - \tau_F^2] + \tau_F^2}}{1 - \beta^2}, \quad \text{with } i=1, 2. \quad (10)$$

As shown in Fig. 1(a) and Table I, the first piece  $\epsilon_1(t)$  has two integration areas: a triangular area below time  $x_1$  and another area under the hyperbola. For the latter area, the  $z_0$ -range is  $[-z_F(x), z_F(x)]$ , where  $\pm z_F(x)$  are the  $z$ -coordinates of the formation time hyperbola at a given time  $x$ :

$$z_F(x) = \sqrt{(t - x)^2 - \tau_F^2}. \quad (11)$$

The second piecewise solution is for time  $t \in [t_a, t_2 + \tau_F]$ , where the formation time hyperbola intersects the upper boundaries of the production area, i.e., the  $z = \pm\beta(x - t_2)$  lines, at time  $x_2$  as given by Eq.(10). As shown in Fig. 1(b), the second piece  $\epsilon_2(t)$  has three integration areas: the lower half of the rhombus (a triangle), the upper half of the rhombus below time  $x_2$  (a trapezoid), and the rhombus above time  $x_2$  but under the hyperbola curve. Note that in each panel of Fig. 1 the different integration areas are separated by the dashed line(s) inside the shaded full integration area. Finally, the third piece  $\epsilon_3(t)$  gives the solution for time  $t \in [t_2 + \tau_F, \infty)$ , where the integration is over  $(z_0, x)$  in the full rhombus.

If we neglect the finite time duration and longitudinal width of the initial energy production and thus make the replacement  $d^3m_T/(dx dz_0 dy) \rightarrow \delta(z_0)\delta(x)dm_T/dy$ , we recover the Bjorken energy density formula of Eq.(1). On the other hand, if we consider the finite time duration

Piece	$t$ range	$x$ range	$z_0$ range
$\epsilon_1(t)$	$[t_1 + \tau_F, t_a]$	$[t_1, x_1]$	$[-\beta(x - t_1), \beta(x - t_1)]$
		$[x_1, t - \tau_F]$	$[-z_F(x), z_F(x)]$
$\epsilon_2(t)$	$[t_a, t_2 + \tau_F]$	$[t_1, t_{\text{mid}}]$	$[-\beta(x - t_1), \beta(x - t_1)]$
		$[t_{\text{mid}}, x_2]$	$[-\beta(t_2 - x), \beta(t_2 - x)]$
		$[x_2, t - \tau_F]$	$[-z_F(x), z_F(x)]$
$\epsilon_3(t)$	$[t_2 + \tau_F, \infty)$	$[t_1, t_{\text{mid}}]$	$[-\beta(x - t_1), \beta(x - t_1)]$
		$[t_{\text{mid}}, t_2]$	$[-\beta(t_2 - x), \beta(t_2 - x)]$

TABLE I. Piecewise solution of  $\epsilon(t)$  for different ranges of time  $t$  together with the corresponding integration limits for the production time  $x$  and production  $z$ -coordinate  $z_0$ .

but neglect the finite longitudinal width and thus make the replacement  $d^3m_T/(dx dz_0 dy) \rightarrow \delta(z_0)d^2m_T/(dx dy)$ , Eq.(5) then reduces to the previously known solution: Eq.(5) of Ref.[17]. Note that  $\epsilon(t)$  is higher for a smaller  $\tau_F$  (at given  $\sqrt{s_{\text{NN}}}$ ,  $A$  and  $t$ ) because the integration area gets bigger, except that the late-time  $\epsilon(t)$  at  $t > t_2 + \tau_F$  does not depend on  $\tau_F$ .

To proceed further, we now consider central Au+Au collisions and specify the function  $d^3m_T/(dx dz_0 dy)$  in Eq.(5). We first assume that the initial transverse mass rapidity density of produced partons per production area can be written in a factorized form:

$$\frac{d^3m_T}{dx dz_0 dy} = g(z_0, x) \frac{dm_T}{dy}. \quad (12)$$

The area density function  $g(z_0, x)$  is normalized as

$$\iint_{S_0} dx dz_0 g(z_0, x) = 1 \quad (13)$$

so that  $dm_T/dy$  represents the initial rapidity density of the transverse mass of all produced partons. We further make the simplest assumption that partons are produced uniformly over the full production area  $S_0$ , i.e.,

$$g(z_0, x) = \frac{2}{\beta t_{21}^2}. \quad (14)$$

We parametrize the initial  $dm_T/dy$  of produced partons as a Gaussian function in rapidity:

$$\frac{dm_T}{dy} = \frac{dm_T}{dy}(0) e^{-\frac{y^2}{2\sigma^2}}, \quad (15)$$

where we use the notation  $F(0)$  to represent the value of  $F(y)$  at  $y = 0$ . We then take the peak value of  $dm_T/dy$  at different collision energies from a parametrization of the results from the string melting version of the AMPT model [17]:

$$\frac{dm_T}{dy}(0) = 168 \left( \frac{\sqrt{s_{\text{NN}}}}{\text{GeV}} - 0.930 \right)^{0.348} \text{ GeV}. \quad (16)$$

To determine the Gaussian width  $\sigma$ , we take advantage of the conservation of energy by assuming that for central

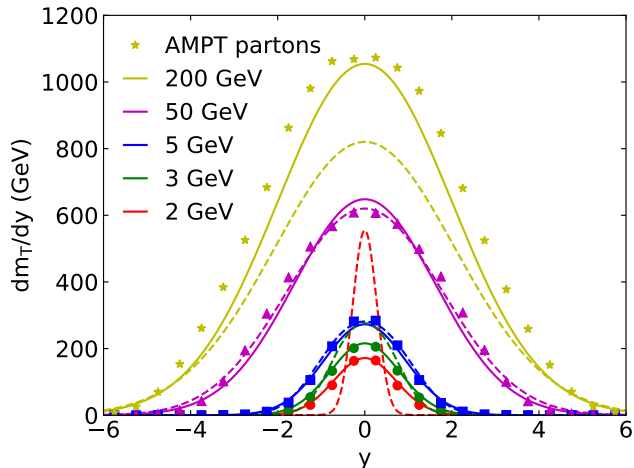


FIG. 2. Parametrized initial rapidity density of transverse mass of produced partons (solid curves) for central Au+Au collisions at  $\sqrt{s_{\text{NN}}} = 2, 3, 5, 50,$  and  $200$  GeV. Symbols represent the results of initial partons from the AMPT model, while dashed curves represent the parametrized hadron  $dm_{\text{T}}/dy$  at these energies.

collisions all incoming nucleons are participant nucleons:

$$\int \frac{dm_{\text{T}}}{dy} \cosh y dy = A\sqrt{s_{\text{NN}}}. \quad (17)$$

We then obtain

$$\sigma = \sqrt{W_0(r^2)}, \quad \text{with } r = \frac{A\sqrt{s_{\text{NN}}}}{\sqrt{2\pi} \frac{dm_{\text{T}}}{dy}(0)}, \quad (18)$$

where  $W_0(x)$  is the  $k = 0$  branch of the Lambert  $W$  function (or the omega function)  $W_k(x)$ . Finally, we can write the initial energy density averaged over the transverse area as

$$\epsilon(t) = \frac{2}{A_{\text{T}}\beta t_{21}^2} \frac{dm_{\text{T}}}{dy}(0) \iint_S \frac{dx dz_0}{t-x} e^{-\frac{y_0^2}{2\sigma^2}} \cosh^3 y_0. \quad (19)$$

Figure 2 shows the  $dm_{\text{T}}/dy$  of produced partons as given by Eq.(15) in central Au+Au collisions at several energies (solid curves), where we see a monotonous increase of the peak value and the Gaussian width with the collision energy. Symbols represent the results of initially produced partons from the string melting version of the AMPT model [17], which show the same qualitative features. Note that in more realistic calculations such as those from the HIJING model [23, 24] or the AMPT model [25] a small fraction of the incoming nucleons are spectators in central collisions.

### III. RESULTS FOR CENTRAL AU+AU COLLISIONS

Our results for  $\epsilon(t)$  depend on choosing specific values for the time parameters  $\tau_{\text{F}}$ ,  $t_1$ , and  $t_2$ . As in the previous

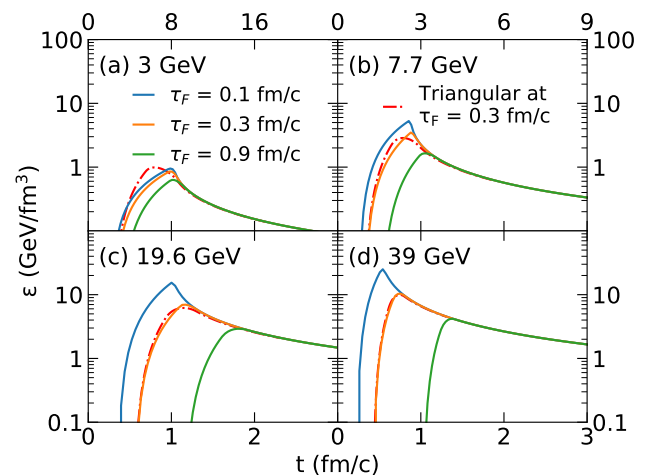


FIG. 3. Energy density of produced partons in central Au+Au collisions at  $\sqrt{s_{\text{NN}}} = 3, 7.7, 19.6,$  and  $39$  GeV for  $\tau_{\text{F}} = 0.1, 0.3$  and  $0.9$  fm/c; the triangular solution for  $\tau_{\text{F}} = 0.3$  fm/c is also shown for comparison.

study [17], we take

$$t_1 = 0.2 d_t, \quad t_2 = 0.8 d_t, \quad (20)$$

instead of the naive choice of  $t_1 = 0$  and  $t_2 = d_t$ ; this is understandable because a boosted nucleus has the shape of an ellipsoid instead of a uniform disk. These particular values are chosen [17] so that the width of the production time distribution is similar to the results from the string melting version of the AMPT model.

Figure 3 shows our results of the initial energy density versus time for central Au+Au collisions at  $\sqrt{s_{\text{NN}}} = 3, 7.7, 19.6,$  and  $39$  GeV in four panels for several different  $\tau_{\text{F}}$  values. We see that the energy density first increases smoothly with time and that the late-time decrease is essentially the same for different  $\tau_{\text{F}}$  values. In addition, the peak energy density increases with the decrease of  $\tau_{\text{F}}$ , but the relative increase is smaller at lower energies. These features are the same as those from the previous study that only includes the finite time duration [17]. Also, our results for  $\tau_{\text{F}} = 0.3$  fm/c are quite close to those from the previous triangular time profile that took the same  $t_1$  and  $t_2$  values [17]. This may be expected because the assumption in Eq.(14) of a uniform distribution in  $(z_0, x)$  leads to a triangular time profile in  $x$  (after integrating over  $z_0$ ). Note that the triangular

solution is also a piecewise solution [17]:

$$\begin{aligned}
\epsilon_{\text{tri}}(t) &= \frac{4}{A_T t_{21}^2} \frac{dm_T}{dy}(0) \left[ -t + t_1 + \tau_F + (t - t_1) \ln \left( \frac{t - t_1}{\tau_F} \right) \right], \\
&\quad \text{for } t \in [t_1 + \tau_F, t_{\text{mid}} + \tau_F]; \\
&= \frac{4}{A_T t_{21}^2} \frac{dm_T}{dy}(0) \left[ t - t_2 - \tau_F + (t - t_1) \ln \left( \frac{t - t_1}{t - t_{\text{mid}}} \right) \right. \\
&\quad \left. + (t_2 - t) \ln \left( \frac{t - t_{\text{mid}}}{\tau_F} \right) \right], \text{ for } t \in [t_{\text{mid}} + \tau_F, t_2 + \tau_F]; \\
&= \frac{4}{A_T t_{21}^2} \frac{dm_T}{dy}(0) \left[ (t - t_1) \ln \left( \frac{t - t_1}{t - t_{\text{mid}}} \right) \right. \\
&\quad \left. + (t_2 - t) \ln \left( \frac{t - t_{\text{mid}}}{t - t_2} \right) \right], \text{ for } t \in [t_2 + \tau_F, \infty). \quad (21)
\end{aligned}$$

Note that  $dm_T/dy(0)$  appears in the above solution because only partons at  $y \approx 0$  can enter the central spacetime-rapidity region of  $\eta_s \approx 0$  when the finite  $z$ -width of the initial energy production is neglected.

From each  $\epsilon(t)$  curve we extract the maximum energy density  $\epsilon^{\text{max}}$ , whose values are shown in Fig. 4(a) as functions of the collision energy for several different  $\tau_F$  values. For our method (solid), the triangular time profile (dot-dashed), or the Bjorken formula (dotted), the three curves from top to bottom represent the results for  $\tau_F = 0.1, 0.3$  and  $0.9$  fm/c, respectively. At high energies and a finite  $\tau_F$  where  $\tau_F \gg d_t$ , one finds that both our solution and the triangular solution reduce to the Bjorken formula, which can be seen in Fig. 4(a). Numerically we observe that the Bjorken  $\epsilon^{\text{max}}$  value starts to be significantly different (by 20% or more) from our finite-thickness result when  $\tau_F/d_t \lesssim 1$  (as we naively expect), which may be considered as the condition when the Bjorken energy density formula breaks down.

At low energies, our  $\epsilon^{\text{max}}$  value is much smaller than that from the Bjorken formula and its dependence on  $\tau_F$  is also much weaker. These qualitative features are the same as those found in the earlier study [17]. Furthermore, we find that numerically  $\tau_F/d_t \lesssim 0.2$  when our  $\epsilon^{\text{max}}$  value is significantly different (by 20% or more) from the previous triangular solution, and usually our  $\epsilon^{\text{max}}$  is smaller than the triangular solution at very low energies but is bigger at intermediate energies. Note that for the triangular time profile of the initial energy production the maximum energy density is given by [17]

$$\begin{aligned}
\epsilon_{\text{tri}}^{\text{max}} &= \frac{2}{A_T t_{21}} \frac{dm_T}{dy}(0) \left[ -1 - \frac{\tau_F}{t_{21}} + \sqrt{\frac{\tau_F}{t_{21}}} \sqrt{2 + \frac{\tau_F}{t_{21}}} \right. \\
&\quad \left. + 2 \ln \left( \frac{1 + \sqrt{1 + 2 t_{21}/\tau_F}}{2} \right) \right]. \quad (22)
\end{aligned}$$

We know that the energy density from the Bjorken formula diverges as  $1/\tau_F$ , while the triangular solution diverges as  $1/\tau_F$  at high energies but as  $\ln(1/\tau_F)$  at low energies [17]. Figure 4(b) shows how the maximum energy density depends on the formation time  $\tau_F$ , where solid curves show our results for central Au+Au collisions at  $\sqrt{s_{\text{NN}}} = 3, 10$  and  $200$  GeV as functions of  $\tau_F$ .

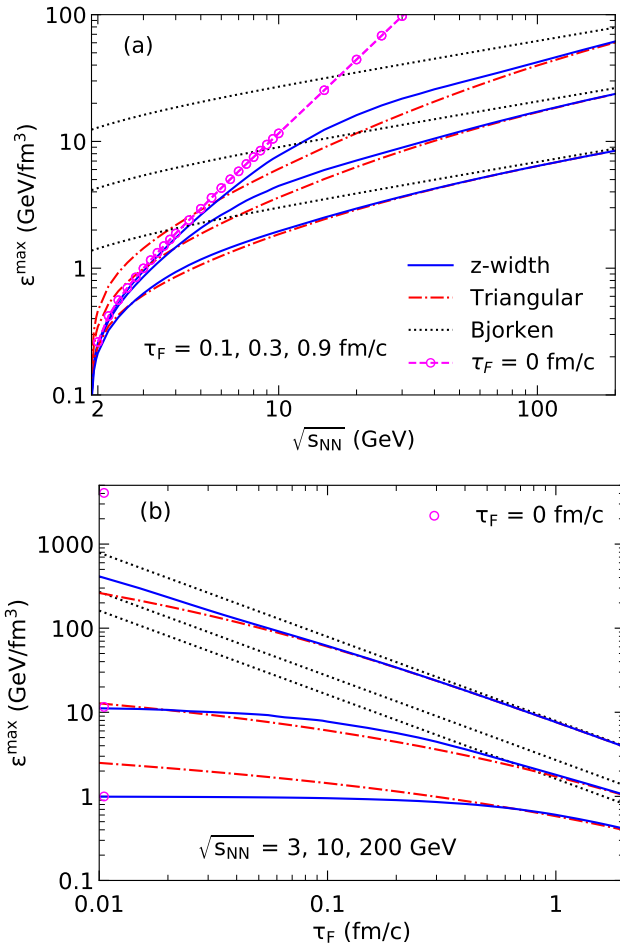


FIG. 4. Maximum energy density for central Au+Au collisions (a) as a function of collision energy at  $\tau_F = 0.1, 0.3$  and  $0.9$  fm/c and (b) as a function of proper formation time at  $\sqrt{s_{\text{NN}}} = 3, 10, 200$  GeV from our method, the triangular time profile, and the Bjorken formula. Circles represent results for  $\tau_F = 0$ .

We see a flattening of  $\epsilon^{\text{max}}$  as  $\tau_F$  decreases towards zero, which is more obvious at lower energies. Also, our results are close to results from the previous triangular solution (dot-dashed) when the formation time is not too small. On the other hand, energy densities from the Bjorken formula (dotted lines) go as  $1/\tau_F$  and are much higher than our results at low energies and/or small  $\tau_F$  values.

#### IV. FINITENESS OF $\epsilon^{\text{max}}$ AT $\tau_F = 0$

We further find that the maximum initial energy density at  $\tau_F = 0$ ,  $\epsilon^{\text{max}}(\tau_F = 0)$ , is finite, and the values are shown as circles in Fig. 4(b) for those three energies. Note that  $\epsilon^{\text{max}}(\tau_F = 0)$  is finite at any energy, and its energy dependence is shown in Fig. 4(a) as the curve with circles. We see that the  $\epsilon^{\text{max}}(\tau_F = 0)$  value is quite close to (within 20% of) the  $\epsilon^{\text{max}}$  value at  $\tau_F = 0.1$  fm/c for

central Au+Au collisions at  $\sqrt{s_{\text{NN}}} \lesssim 7$  GeV.

As an analytical proof of the finiteness of  $\epsilon^{\text{max}}(\tau_{\text{F}} = 0)$ , next we derive its upper bound. Equation (4) allows us to write

$$z_0 = -r_0 \sinh y_0, \quad t - x = r_0 \cosh y_0 \quad (23)$$

for partons that contribute to the energy density  $\epsilon(t)$  at  $\eta_s \approx 0$ . For brevity we write the variable  $y_0$  as  $y$  in the rest of this section, we can then write Eq.(19) as

$$\begin{aligned} \epsilon(t) &= \frac{2}{A_{\text{T}}\beta t_{21}^2} \iint_S \frac{dm_{\text{T}}}{dy} \cosh^2 y \, dr_0 dy \\ &= \frac{2}{A_{\text{T}}\beta t_{21}^2} \int \frac{dm_{\text{T}}}{dy} \cosh^2 y \Delta r_0(y) dy, \end{aligned} \quad (24)$$

where  $\Delta r_0(y) \equiv r_0^{\text{max}}(y) - r_0^{\text{min}}(y)$ . By analyzing the general crossing diagram (i.e., the one using  $t_1$  and  $t_2$ ) similar to Fig. 1, we first find that for  $t \leq t_2$  we always have

$$r_0^{\text{min}}(y) = 0, \quad r_0^{\text{max}}(y) \leq r_1(y), \quad (25)$$

for a given parton rapidity  $y$  when  $\tau_{\text{F}} = 0$ . In the above,  $r_1(y)$  is the  $r_0$  value when a parton passing through the observation point  $(0, t)$  with rapidity  $y$  intersects one of the  $z = \pm\beta(x - t_1)$  lines in the general crossing diagram:

$$r_1(y) = \frac{\beta(t - t_1)}{\beta \cosh y + |\sinh y|}. \quad (26)$$

Thus for  $t \leq t_2$  we have

$$\Delta r_0(y) \leq \frac{\beta t_{21}}{\beta \cosh y + |\sinh y|}. \quad (27)$$

Secondly, for  $t \geq t_2$  we can obtain

$$\Delta r_0(y) = \frac{\beta \cosh y t_{21} - 2|\sinh y|(t - t_{\text{mid}})}{\beta \cosh^2 y - \sinh^2 y / \beta}, \quad (28)$$

which also satisfies the inequality of Eq.(27). Equation (24) then gives

$$\epsilon(t) \leq \frac{2}{A_{\text{T}}t_{21}} \frac{dm_{\text{T}}}{dy}(0) \int e^{-\frac{y^2}{2\sigma^2}} \frac{\cosh^2 y \, dy}{\beta \cosh y + |\sinh y|} \equiv \epsilon_{\text{bound}}. \quad (29)$$

This upper bound of the energy density is shown (thick dashed curve) for central Au+Au collisions as a function of the collision energy in Fig. 5. We observe that it approaches the  $\epsilon^{\text{max}}(\tau_{\text{F}} = 0)$  value (the top solid curve) at high energies. Note that as  $\beta \rightarrow 1$  the light cone boundaries overlap with the upper boundaries of the rhombus production area, thus the inequality of Eq.(27) becomes an equality for  $t \leq t_2$  but not for  $t > t_2$ . Therefore the observation  $\epsilon_{\text{bound}} \rightarrow \epsilon^{\text{max}}(\tau_{\text{F}} = 0)$  at high energies suggests that the maximum energy density for  $\tau_{\text{F}} = 0$  is reached at  $t \leq t_2$ . This is the case for the triangular time profile [17], where  $\epsilon_{\text{tri}}^{\text{max}} = \epsilon_{\text{tri}}(t =$

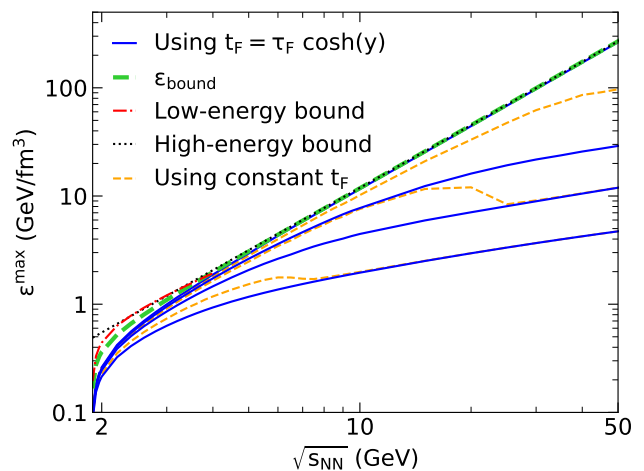


FIG. 5. Maximum energy density for central Au+Au collisions as a function of collision energy at  $\tau_{\text{F}} = 0, 0.1, 0.3$  and  $0.9$  fm/c in comparison with the upper bound of  $\epsilon^{\text{max}}$  of Eq.(29), where the analytical low- and high-energy bounds are also shown. Dashed curves represent the  $\epsilon^{\text{max}}$  results when using a constant formation time  $t_{\text{F}} = 0.1, 0.3,$  and  $0.9$  fm/c.

$t_{\text{mid}} + \tau_{\text{F}}/2 + \sqrt{\tau_{\text{F}}\sqrt{2} t_{21} + \tau_{\text{F}}/2}$ ) occurs at a time within  $[t_{\text{mid}} + \tau_{\text{F}}, t_2 + \tau_{\text{F}})$ .

For an explicit analytical expression of the upper bound, we take advantage of

$$\frac{1}{\beta \cosh y + |\sinh y|} \leq \frac{e^{-|y|}}{\beta}. \quad (30)$$

Using Eq.(18), we then reduce Eq.(29) to

$$\epsilon(t) \leq \frac{A\sqrt{s_{\text{NN}}}}{2A_{\text{T}}\beta t_{21}} \left[ 2 + \text{erfc}\left(\frac{\sigma}{\sqrt{2}}\right) + e^{4\sigma^2} \text{erfc}\left(\frac{3\sigma}{\sqrt{2}}\right) \right], \quad (31)$$

where  $\text{erfc}(x)$  is the complementary error function. The right hand side of Eq.(31) can be considered as the high energy expression of the upper bound, and as shown in Fig. 5 (dotted curve) it agrees well with  $\epsilon_{\text{bound}}$  of Eq.(29) for  $\sqrt{s_{\text{NN}}} > 4$  GeV. For very low energies, however, the relaxation of Eq.(30) is too loose and thus the high energy bound of Eq.(31) fails to approach zero at the threshold energy.

At very low energies where  $\beta \ll 1$ , we find from Eq.(18) that  $\sigma < 0.707$  for  $\sqrt{s_{\text{NN}}} < 1.96$  GeV. Using the fact  $\exp(-y^2/2\sigma^2) \cosh^2 y \leq 1$  for  $\sigma < 1/\sqrt{2}$ , Eq.(29) gives

$$\begin{aligned} \epsilon(t) &\leq \frac{2}{A_{\text{T}}t_{21}} \frac{dm_{\text{T}}}{dy}(0) \int \frac{dy}{\beta \cosh y + |\sinh y|} \\ &= \frac{8}{A_{\text{T}}t_{21}\sqrt{1-\beta^2}} \frac{dm_{\text{T}}}{dy}(0) \tanh^{-1}\left(\sqrt{\frac{1-\beta}{1+\beta}}\right). \end{aligned} \quad (32)$$

This low energy expression of the upper bound is shown in Fig. 5 (dot-dashed curve), where we see that it captures the decrease of the energy density  $\epsilon^{\text{max}}(\tau_{\text{F}} = 0)$  towards the threshold energy. Note that  $\epsilon_{\text{bound}} \propto \beta \ln(2/\beta)$

at very low energies according to Eq.(32), therefore the peak energy density goes towards zero as the collision energy approaches the threshold although the initial transverse mass rapidity density of Eq.(16) is always finite.

## V. SCALING AND $A$ -DEPENDENCE OF $\epsilon(t)$

Our solution of Eq.(19) has an approximate scaling property. We first note that, in the hard sphere model of the nucleus, both the time duration  $d_t$  and the  $z$ -width of the production area are proportional to  $A^{1/3}$ . Secondly, we can expect  $dm_T/dy(0)$  to be approximately proportional to the number of participant nucleons and thus proportional to  $A$  for central collisions; this is the case for the parametrization of the final hadron  $dE_T/dy$  by the PHENIX Collaboration [22]. If  $dm_T/dy(0) \propto A$  for central collisions, Eq.(18) means that the Gaussian width  $\sigma$  of the  $dm_T/dy$  distribution is independent of  $A$ .

Next we define the scaled time and scaled proper formation time respectively as

$$t^s = \frac{t}{A^{1/3}}, \quad \tau_F^s = \frac{\tau_F}{A^{1/3}}. \quad (33)$$

Under these approximations (i.e.,  $d_t$  and the  $z$ -width of the production area are proportional to  $A^{1/3}$  and  $dm_T/dy(0) \propto A$ ), we see from Eq.(19) that at a given collision energy  $\epsilon(t)$  is only a function of  $t^s$  and  $\tau_F^s$ , while  $\epsilon^{\max}$  is only a function of  $\tau_F^s$ . This also gives the following scaling relation:

$$\epsilon_{AA}^{\max}(\text{for } \tau_F) = \epsilon_{\text{AuAu}}^{\max} \left( \text{for } \tau_F^{\text{Au}} = (197/A)^{1/3} \tau_F \right) \quad (34)$$

at the same energy ( $\sqrt{s_{NN}}$ ). For example, it means  $\epsilon_{\text{OO}}^{\max}(\text{for } \tau_F = 0.30 \text{ fm}/c) = \epsilon_{\text{AuAu}}^{\max}(\text{for } \tau_F = 0.69 \text{ fm}/c)$  for central collisions at the same energy. In addition, it means that  $\epsilon_{AA}^{\max}(\tau_F = 0)$  only depends on  $\sqrt{s_{NN}}$  but not on  $A$ . If one were willing to apply these approximations down to  $A = 1$  (for the proton), Eq.(34) would give  $\epsilon_{AA}^{\max}(\tau_F = 0) = \epsilon_{pp}^{\max}(\tau_F = 0)$  for central  $AA$  collisions at the same energy.

Furthermore, the scaling means that the  $\tau_F$ -dependence of  $\epsilon^{\max}$  at a given energy, such as the curves shown in Fig. 4(b), also gives the  $A$ -dependence of  $\epsilon^{\max}$  for central collisions. We see that the Bjorken formula Eq.(1) and the triangular solution Eq.(21) also satisfy the scaling relation. However, different  $\tau_F$ -dependences correspond to different  $A$ -dependences of the maximum energy density. For example, at low energies our result has a very flat  $\tau_F$ -dependence as shown in Fig. 4(b), which translates to a very slow increase of  $\epsilon^{\max}$  with  $A$ . At finite  $\tau_F$  and high-enough energies, however, our result reduces to the Bjorken energy density formula, where  $\epsilon^{\max} \propto A^{1/3}$  at fixed  $\tau_F$ . Also note that under the same approximations the upper bound of the energy density  $\epsilon_{\text{bound}}$  in Eq.(29) is independent of  $A$ , just like  $\epsilon_{AA}^{\max}(\tau_F = 0)$ .

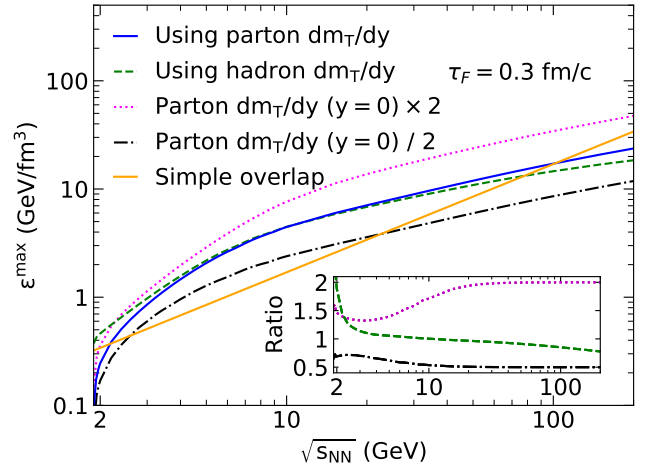


FIG. 6. Maximum energy density using the parton  $dm_T/dy$ , the hadron  $dm_T/dy$ , or modified parton  $dm_T/dy$  (see text for details) for  $\tau_F = 0.3 \text{ fm}/c$  as functions of energy. The inset shows ratios of  $\epsilon^{\max}$  from various  $dm_T/dy$  profiles to  $\epsilon^{\max}$  from the default parton  $dm_T/dy$ , while the solid straight line shows the energy density if two boosted nuclei simply overlap.

## VI. DISCUSSIONS

In the calculations of energy density with Eq.(19) so far, we have taken  $dm_T/dy$  as the transverse mass rapidity density of initial partons, which peak value as a function of energy is parametrized according to results from the AMPT model [17, 25]. To investigate the uncertainty of the energy density due to  $dm_T/dy$ , we could also take  $dm_T/dy$  as the transverse mass rapidity density of final hadrons. The hadron  $dm_T/dy$  is derived in the Appendix and shown in Fig. 2 (dashed curves) for central Au+Au collisions at several energies. We see that the hadron  $dm_T/dy$  and parton  $dm_T/dy$  are similar at energies between  $\approx 3$  and 50 GeV. At 2 GeV near the threshold energy, however, the hadron  $dm_T/dy$  has a higher peak but is narrower than the parton  $dm_T/dy$  because of the slow baryons, while the hadron  $dm_T/dy$  has a lower peak at the top RHIC energy consistent with the effect of strong secondary interactions. Note that both the hadron and parton  $dm_T/dy$  satisfy the energy conservation of Eq.(17).

Figure 6 shows the  $\epsilon^{\max}$  values in central Au+Au collisions as functions of energy when the hadron  $dm_T/dy$  is used (dashed curve) for  $\tau_F = 0.3 \text{ fm}/c$ . We see that it is rather close to our result for the parton  $dm_T/dy$  (solid curve) within  $3 < \sqrt{s_{NN}} < 100 \text{ GeV}$ . At high energies the production area is relatively small compared to the finite  $\tau_F$ , so partons with rapidities near zero dominate the energy at  $\eta_s \approx 0$ . Therefore  $\epsilon^{\max}$  at high collision energies is expected to depend mostly on  $dm_T/dy(0)$ ; as a result, the  $\epsilon^{\max}$  value using the hadron  $dm_T/dy$  is lower than that using the parton  $dm_T/dy$  (see Fig. 2). At low energies particles at finite rapidities can also contribute

significantly to the energy at  $\eta_s \approx 0$ , thus  $\epsilon^{\max}$  depends on not only  $dm_T/dy(0)$  but also the Gaussian width  $\sigma$ . To further demonstrate this, we have changed the parton  $dm_T/dy(0)$  value by a factor of 2 and then determined the Gaussian width with the energy conservation of Eq.(17); the corresponding  $\epsilon^{\max}$  values are shown in Fig. 6 with the ratio over our default result (solid curve) shown in the inset. We see that the change of  $\epsilon^{\max}$  is the same factor of 2 at high energies but is smaller than two at low energies.

We also show in Fig. 6 the simplest estimate for the energy density (straight line), where one imagines the two boosted nuclei to simply overlap in volume with all interactions neglected. In the hard sphere model of the nucleus, this energy density would be

$$\epsilon^{\text{overlap}} = \frac{3\sqrt{s_{\text{NN}}}}{4\pi R_1^3}, \quad (35)$$

which grows linearly with  $\sqrt{s_{\text{NN}}}$  but is independent of  $A$ . Naively we expect the actual maximum energy density in the central spacetime-rapidity region to be higher than  $\epsilon^{\text{overlap}}$  due to the compression from the primary nucleus-nucleus collision. This is indeed the case in Fig. 6 except for very low or very high energies. Near the threshold energy the energy density using the hadron  $dm_T/dy$  is higher than  $\epsilon^{\text{overlap}}$ , but the energy density using the parton  $dm_T/dy$  is lower. However, a parton matter is unlikely to be formed near the threshold energy due to the low estimated energy density, therefore the hadron  $dm_T/dy$  should be more applicable there. At very high energies, we expect the parton  $dm_T/dy$  to be applicable but the maximum energy density is lower than  $\epsilon^{\text{overlap}}$ . This is because of the finite formation time  $\tau_F$ ; for example we see from Fig. 4(a) that the peak energy density at  $\tau_F = 0$  at high energies is always bigger than  $\epsilon^{\text{overlap}}$ .

We have also considered a scenario where all initial partons have the same formation time  $t_F$  instead of the same proper formation time  $\tau_F$ . The energy density is still given by Eqs.(5) and (19), but the formation time requirement restricts the integration area  $S$  to  $x \leq t - t_F$  instead of restricting  $S$  below the proper time hyperbola of Eq.(7). Figure 5 shows the  $\epsilon^{\max}$  results (thin dashed curves) for  $t_F = 0.1, 0.3$  and  $0.9$  fm/c as functions of energy, where the result above a certain energy (which corresponds to  $\beta t_{21}/2 \approx t_F$ ) is the same as our standard result that takes the same value for  $\tau_F$ . However, just below this energy scale we see a strange decrease of  $\epsilon^{\max}$  with  $\sqrt{s_{\text{NN}}}$ . We find that this is a consequence of a double-peak structure of  $\epsilon(t)$  below this energy scale in the constant- $t_F$  case, where partons at very large rapidities could also contribute to the energy density.

## VII. CONCLUSION

We present a method to calculate the initial energy density produced in heavy ion collisions that takes into

account the finite nuclear thickness. Our method includes both the finite longitudinal ( $z$ -) width and the finite time duration  $d_t$  of the initial energy production. This is a continuation of a previous study that considers the finite duration time (but not the finite  $z$ -width) in an extension of the Bjorken energy density formula. We find the same qualitative conclusions: the initial energy density after considering the finite nuclear thickness approaches the Bjorken formula at large formation time  $\tau_F$  and/or high energies; at low energies, however, the initial energy density has a much lower maximum, evolves much longer, and is much less sensitive to  $\tau_F$  than the Bjorken formula. Numerically we find that the Bjorken energy density formula breaks down (i.e., is different by 20% or more from our results that include the finite nuclear thickness) when  $\tau_F/d_t \lesssim 1$ , as one may expect. When the proper formation time  $\tau_F$  is not too much smaller than the crossing time of the two nuclei, our results are similar to the previous extension results that only include the finite time duration. Numerically we find  $\tau_F/d_t \lesssim 0.2$  when our result is significantly different (by 20% or more) from the previous result.

A qualitative difference from previous studies is that we find the energy density  $\epsilon(t)$  including its maximum  $\epsilon^{\max}$  to be finite at  $\tau_F = 0$  at any energy. In contrast, the Bjorken energy density formula is divergent where  $\epsilon^{\max} \propto 1/\tau_F$  as  $\tau_F \rightarrow 0$ , while the previous study that neglects the finite  $z$ -width gives a  $\ln(1/\tau_F)$  divergence at low energies but the same  $1/\tau_F$  divergence at high energies.

In addition, we find that our  $\epsilon(t)$  results (as well as the Bjorken energy density formula and the previous extension results) for central heavy ion collisions satisfy a scaling relation under two reasonable assumptions. They include the assumption that the initial rapidity density of the transverse energy is proportional to the number of participant nucleons and that the  $z$ -width and time duration  $d_t$  are both proportional to  $A^{1/3}$ . As a result of the scaling, the  $\tau_F$ -dependence of  $\epsilon^{\max}$  for a given  $A$  also determines the  $A$ -dependence of  $\epsilon^{\max}$  (at the same collision energy), therefore the weaker  $\tau_F$ -dependence of our results at low energies means a slower increase of the energy density with the mass number  $A$ . In particular, the scaling means that the  $\epsilon^{\max}$  value at  $\tau_F = 0$  is independent of  $A$  and only depends on the collision energy.

## Appendix A: $dm_T/dy$ of final state hadrons

In the PHENIX Collaboration's data-based parametrization [22] of the transverse energy pseudo-rapidity density around  $\eta = 0$ , the "transverse energy"  $E_T$  is defined as  $E_T = \sum_i E_i \sin \theta_i$ , where  $\theta_i$  is the polar angle of particle  $i$ .  $E_i$  is defined as  $E_i^{\text{tot}} - m_N$  for baryons,  $E_i^{\text{tot}} + m_N$  for antibaryons, and  $E_i^{\text{tot}}$  for all other particles, where  $E_i^{\text{tot}}$  is the total energy of the particle and  $m_N$  is the nucleon mass. As a result of the  $E_T$  definition, the total transverse energy of hadrons at

$y = 0$  is given by

$$\frac{dm_T}{dy} = \frac{dE_T}{dy} + m_N \frac{dN_{\text{netB}}}{dy}, \quad (\text{A1})$$

where  $N_{\text{netB}}$  represents the net-baryon number.

To determine the hadron  $dm_T/dy$  function for calculating the energy density via Eq.(19), we assume that  $dE_T/dy$  is a single Gaussian while  $dN_{\text{netB}}/dy$  can be described with a double-Gaussian [26, 27]:

$$\begin{aligned} \frac{dE_T}{dy} &= \frac{dE_T}{dy}(0) e^{-\frac{y^2}{2\sigma_1^2}}, \\ \frac{dN_{\text{netB}}}{dy} &= C \left( e^{-\frac{(y+y_B)^2}{2\sigma_2^2}} + e^{-\frac{(y-y_B)^2}{2\sigma_2^2}} \right). \end{aligned} \quad (\text{A2})$$

First, regarding  $dE_T/dy(0)$  the PHENIX Collaboration has parametrized the mid-pseudorapidity data as [22]

$$\begin{aligned} \frac{dN_{\text{ch}}}{d\eta}(0) &= 0.37N_p \ln \left( \frac{\sqrt{s_{\text{NN}}}}{1.48\text{GeV}} \right), \\ \frac{dE_T}{d\eta}(0) &= 0.365N_p \ln \left( \frac{\sqrt{s_{\text{NN}}}}{2.35\text{GeV}} \right) \text{ GeV}, \end{aligned} \quad (\text{A3})$$

where  $N_p$  is the number of participants (taken as  $2A$  for central collisions in this study). However, the  $dE_T/d\eta(0)$  parametrization underestimates the  $dE_T/d\eta/(dN_{\text{ch}}/d\eta)$  ratio at energies below  $\sqrt{s_{\text{NN}}} \approx 10$  GeV [22], as shown in Fig. 7(a). Since the effect of finite nuclear thickness is more important at lower energies and the PHENIX parametrization of  $dN_{\text{ch}}/d\eta(0)$  is accurate down to lower energies than that of  $dE_T/d\eta(0)$ , we improve the  $dE_T/d\eta(0)$  parametrization. Specifically, we take the same  $dN_{\text{ch}}/d\eta(0)$  parametrization [22] but refit the  $dE_T/d\eta/(dN_{\text{ch}}/d\eta)$  data at  $\sqrt{s_{\text{NN}}} < 20$  GeV to obtain

$$\frac{dE_T}{d\eta}(0) = 0.308N_p \ln^{1.08} \left( \frac{\sqrt{s_{\text{NN}}}}{E_0} \right) \text{ GeV}, \quad (\text{A4})$$

for  $\sqrt{s_{\text{NN}}} \leq 20.7$  GeV, where  $E_0 = 2m_N$  is the threshold energy. As shown in Fig. 7(a), our improved low energy parametrization intersects the PHENIX parametrization at  $\sqrt{s_{\text{NN}}} \approx 20.7$  GeV, above which we use the PHENIX  $dE_T/d\eta(0)$  parametrization. We then take  $dE_T/dy(0) = 1.25 dE_T/d\eta(0)$  [22], which are shown in Fig. 7(b) for our improved parametrization (thin solid curve) and the PHENIX parametrization (dashed curve).

Next, to specify  $dN_{\text{netB}}/dy$  in Eq.(A2) we first parametrize  $y_B$  and  $\sigma_2$  using the net-proton rapidity density data in central Au+Au collisions (with the exception that central Pb+Pb data are used at 17.3 GeV). For collision energies below 5 GeV, there is little anti-baryon production and thus we use the proton  $dN/dy$  for net-protons at  $\sqrt{s_{\text{NN}}} = 2.4, 3.1, 3.6,$  and  $4.1$  GeV [28]. We also use the net-proton  $dN/dy$  data at  $\sqrt{s_{\text{NN}}} = 5$  GeV

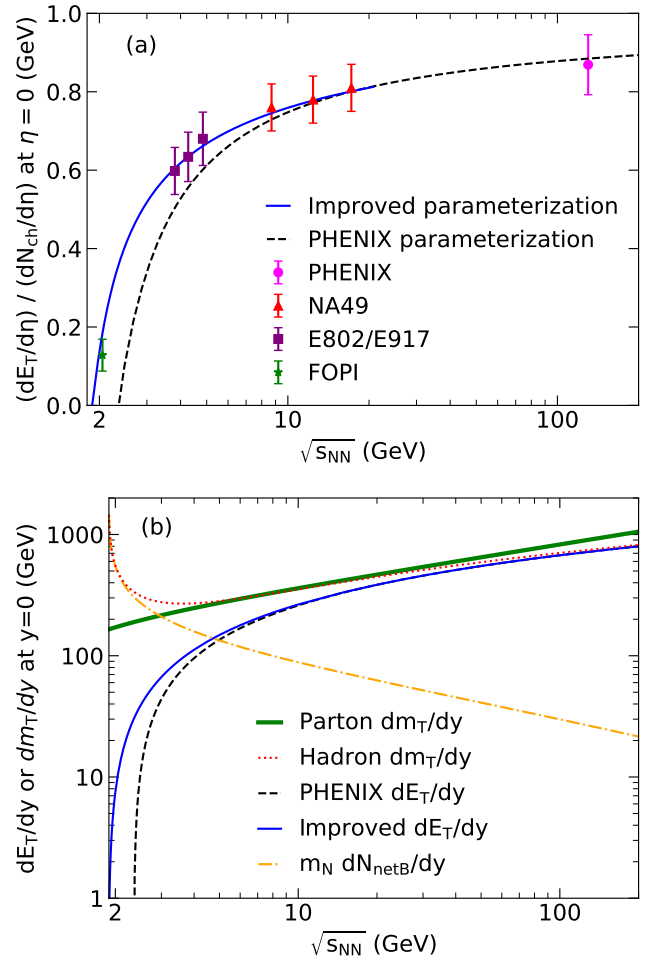


FIG. 7. (a)  $(dE_T/d\eta)/(dN_{\text{ch}}/d\eta)$  data at  $\eta \approx 0$  compared with our improved parametrization below 20.7 GeV and the PHENIX parametrization. (b) Mid-rapidity  $dm_T/dy$  of initial partons and final hadrons for central Au+Au collisions as functions of energy; the net-baryon contribution to the hadron  $dm_T/dy(0)$  as well as the PHENIX parametrization and our improved parametrization of  $dE_T/dy(0)$  are also shown.

[29, 30], 17.3 GeV [31] and 200 GeV [32]. From these data we obtain the following parametrization:

$$\begin{aligned} y_B &= 0.541 \left( \frac{\sqrt{s_{\text{NN}}} - E_0}{\text{GeV}} \right)^{0.196} \ln^{0.392} \left( \frac{\sqrt{s_{\text{NN}}}}{E_0} \right), \\ \sigma_2 &= 0.601 \left( \frac{\sqrt{s_{\text{NN}}} - E_0}{\text{GeV}} \right)^{0.121} \ln^{0.241} \left( \frac{\sqrt{s_{\text{NN}}}}{E_0} \right). \end{aligned} \quad (\text{A5})$$

We further assume that the net-baryon and net-proton  $dN/dy$  distributions have the same shape. We then impose the conservation of the net-baryon number,  $\int (dN_{\text{netB}}/dy) dy = 2A$  to determine the parameter  $C$  in Eq.(A2) at each collision energy. Figure 8 shows the net-proton data at several energies in comparison with our  $dN_{\text{netB}}/dy$  parametrization (scaled down by various factors for better comparison of the shapes). Note that the 5 GeV data shown in Fig. 8 include those from the E802

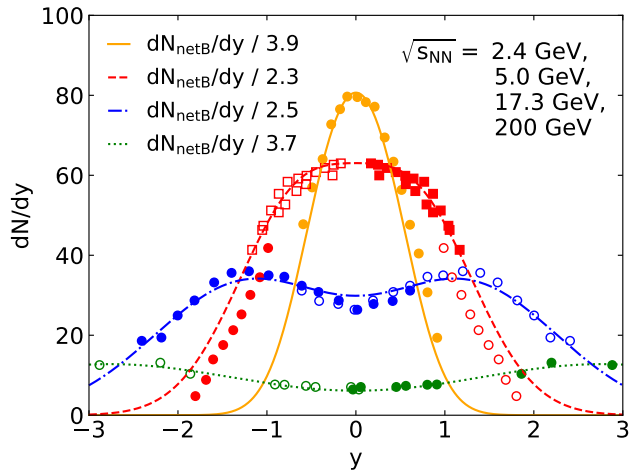


FIG. 8. Net-proton  $dN/dy$  data (circles) for central Au+Au (Pb+Pb) at  $\sqrt{s_{NN}} = 2.4, 5, (17.3),$  and 200 GeV in comparison with the scaled net-baryon parametrization (curves). Filled circles represent actual data and open circles are reflected data across  $y = 0$ .

Collaboration (squares) [29] and the E877 Collaboration

(circles) [30]. Lastly, we calculate the last parameter  $\sigma_1$  in Eq.(A2) by using the conservation of total energy of Eq.(17).

Figure 7(b) shows the energy dependence of our hadron  $dm_T/dy(0)$  parametrization (dotted curve) in comparison with that of the  $dm_T/dy(0)$  for initial partons (thick solid curve). We see that they are rather close within  $3 < \sqrt{s_{NN}} < 100$  GeV, which includes the energy range of the Beam Energy Scan program at RHIC [6–9]. Note the fast increase of hadron  $dm_T/dy(0)$  when  $\sqrt{s_{NN}}$  decreases towards the threshold energy; this is a combined effect of the vanishing beam rapidity near the threshold energy and the finite conserved net-baryon number. It is also clear that at very low energies the net-baryon contribution (dot-dashed curve), coming mostly from the incoming nucleons, dominates the total transverse energy of final hadrons.

## ACKNOWLEDGMENTS

This work has been partially supported by the National Science Foundation under Grant No. 2012947.

- 
- [1] M. Gyulassy and L. McLerran, Nucl. Phys. A **750**, 30-63 (2005).
- [2] I. Arsene *et al.* [BRAHMS Collaboration], Nucl. Phys. A **757**, 1-27 (2005).
- [3] B. B. Back, *et al.* [PHOBOS Collaboration], Nucl. Phys. A **757**, 28-101 (2005).
- [4] J. Adams *et al.* [STAR Collaboration], Nucl. Phys. A **757**, 102-183 (2005).
- [5] K. Adcox *et al.* [PHENIX Collaboration], Nucl. Phys. A **757**, 184-283 (2005).
- [6] B. Mohanty [STAR Collaboration], J. Phys. G **38**, 124023 (2011).
- [7] X. Luo and N. Xu, Nucl. Sci. Tech. **28**, 112 (2017).
- [8] L. Adamczyk *et al.* [STAR Collaboration], Phys. Rev. C **96**, 044904 (2017).
- [9] D. Keane, J. Phys. Conf. Ser. **878**, 012015 (2017).
- [10] M. A. Stephanov, Phys. Rev. Lett. **107**, 052301 (2011).
- [11] A. Bzdak, S. Esumi, V. Koch, J. Liao, M. Stephanov and N. Xu, Phys. Rept. **853**, 1-87 (2020).
- [12] Z. Li, K. Xu, X. Wang and M. Huang, Eur. Phys. J. C **79**, 245 (2019).
- [13] M. Okai, K. Kawaguchi, Y. Tachibana and T. Hirano, Phys. Rev. C **95**, 054914 (2017).
- [14] C. Shen, G. Denicol, C. Gale, S. Jeon, A. Monnai and B. Schenke, Nucl. Phys. A **967**, 796-799 (2017).
- [15] L. Du, U. Heinz and G. Vujanovic, Nucl. Phys. A **982**, 407-410 (2019).
- [16] J. D. Bjorken, Phys. Rev. D **27**, 140-151 (1983).
- [17] Z. W. Lin, Phys. Rev. C **98**, 034908 (2018).
- [18] Z. W. Lin, Phys. Rev. C **90**, 014904 (2014).
- [19] Z. Xu and C. Greiner, Phys. Rev. C **71**, 064901 (2005).
- [20] K. Kajantie, R. Raitio and P. V. Ruuskanen, Nucl. Phys. B **222**, 152-188 (1983).
- [21] C. Spieles, R. Vogt, L. Gerland, S. A. Bass, M. Bleicher, H. Stöcker and W. Greiner, Phys. Rev. C **60**, 054901 (1999).
- [22] S. Adler *et al.* [PHENIX Collaboration], Phys. Rev. C **71**, 034908 (2005).
- [23] X. N. Wang and M. Gyulassy, Phys. Rev. D **44**, 3501-3516 (1991).
- [24] M. Gyulassy and X. N. Wang, Comput. Phys. Commun. **83**, 307 (1994).
- [25] Z. W. Lin, C. M. Ko, B. A. Li, B. Zhang and S. Pal, Phys. Rev. C **72**, 064901 (2005).
- [26] T. Anticic *et al.* [NA49 Collaboration], Phys. Rev. Lett. **93**, 022302 (2004).
- [27] Y. Mehtar-Tani and G. Wolschin, Phys. Rev. Lett. **102**, 182301 (2009).
- [28] J. Klay *et al.* [E895 Collaboration], Phys. Rev. Lett. **88**, 102301 (2002).
- [29] L. Ahle *et al.* [E802 Collaboration], Phys. Rev. C **60**, 064901 (1999).
- [30] J. Barrette *et al.* [E877 Collaboration], Phys. Rev. C **62**, 024901 (2000).
- [31] H. Appelshauser *et al.* [NA49 Collaboration], Phys. Rev. Lett. **82**, 2471-2475 (1999).
- [32] I. Bearden *et al.* [BRAHMS Collaboration], Phys. Rev. Lett. **93**, 102301 (2004).